NIH Public Access
Author Manuscript
IEEE Trans Biomed Eng. Author manuscript; available in PMC 2011 January 1.

Published in final edited form as:
IEEE Trans Biomed Eng. 2010 January ; 57(1): 155–166. doi:10.1109/TBME.2009.2029703.

Spatial and Temporal Controlled Tissue Heating on a Modified Clinical Ultrasound Scanner for Generating Mild Hyperthermia in Tumors

Dustin E. Kruse[1], **Chun-Yen Lai**[1], **Douglas N. Stephens**[1], **Patrick Sutcliffe**[2], **Eric E. Paoli**[1], **Stephen H. Barnes**[2], and **Katherine W. Ferrara**[1]

[1] University of California at Davis, Department of Biomedical Engineering, Davis, CA

[2] Siemens Corporate Research, Inc., Image Processing Department, Issaquah, WA

Abstract

A new system is presented for generating controlled tissue heating with a clinical ultrasound scanner, and initial *in vitro* and *in vivo* results are presented that demonstrate both transient and sustained heating in the mild-hyperthermia range of 37–42ºC. The system consists of a Siemens Antares™ ultrasound scanner, a custom dual-frequency 3-row transducer array and an external temperature feedback control system. The transducer has 2 outer rows that operate at 1.5 MHz for tissue heating and a center row that operates at 5 MHz for B-mode imaging to guide the therapy. We compare the field maps obtained using a hydrophone against calculations of the ultrasound beam based on monochromatic and linear assumptions. Using the finite-difference time-domain (FDTD) method, we compare predicted time-dependent thermal profiles to measured profiles for soy tofu as a tissue-mimicking phantom. *In vitro* results show differential heating of 6ºC for chicken breast and tofu. *In vivo* tests of the system were performed on three mice bearing Met-1 tumors, which is a model of aggressive, metastatic and highly vascular breast cancer. In superficially implanted tumors, we demonstrate controlled heating to 42ºC. We show that the system is able to maintain the temperature to within 0.1ºC of the desired temperature both *in vitro* and *in vivo*.

I. INTRODUCTION

The absorption of propagating ultrasound waves increases tissue temperature [3,4]. Significant temperature elevations in soft tissues (on the order of 1ºC) are possible for non-scanned beams within acoustic exposure parameters set by the FDA for ultrasound imaging [5,6]. Perhaps the most common use of high intensity ultrasound is in tissue ablation, in which a sufficient thermal dose is delivered to damage cells irreversibly, e.g. in tumors. High-intensity focused-ultrasound (HIFU) is FDA-approved for the ablation of uterine fibroids [7]. In the HIFU application, MRI is used for both treatment planning as well as thermometry in 3-spatial dimensions plus time, which yields excellent spatio-temporal control [9]. While MR guidance may provide a 3D view of a wide region of interest, guiding treatment with ultrasound is attractive due to the lower cost and simplicity. Even when MRI and ultrasound are combined, the incorporation of a combined ultrasound imaging and therapy array may facilitate pre-clinical studies of thermal therapies.

For cancer treatment, the application of mild-hyperthermia, where temperatures are elevated by 1 to 5°C for short intervals, may be an important use of ultrasound heating. Several effects have been reported as a result of mild-hyperthermia in tumors, including increased vascular permeability [10], increased blood flow [11], increased oxygenation [12], and decreased pH [13]. Additionally, a recent study shows that mild-hyperthermia increases the effectiveness of chemotherapy and radiotherapy [14]. Moreover, there is intense research in the synthesis of

NIH-PA Author Manuscript
NIH-PA Author Manuscript
NIH-PA Author Manuscript

NIH-PA Author Manuscript

NIH-PA Author Manuscript

NIH-PA Author Manuscript

thermally-sensitive drug delivery vehicles, which are engineered to release a drug payload in a narrow temperature range, typically between 39 and 41°C [15]. For such applications, it is important to consider thermal dose since cellular mortality follows an Arrhenius relationship as a function of both temperature and time [16]. Thermal dose is often estimated in terms of the cumulative equivalent minutes at 43°C (CEM43). CEM 43 is defined as $tR^{(43-T)}$, with t being the time of treatment, T the average temperature during treatment, and R a constant that equals 0.25 for temperatures between 37 and 43°C [12,17] and 0.5 above 43°C. For mild hyperthermia, it is necessary to maintain the thermal dose at a CEM43 below 0.5 min in order to prevent irreversible thermal damage.

The objective of the work presented in this paper is to implement and test a new system capable of spatial and temporal control of ultrasound heating for cancer therapy. In our first implementation of controlled tissue heating, we employed an imaging array mechanically aligned with a high power focused transducer. Here, rather than the typical bottom-up approach where separate systems are tied together, we chose to implement a top-down approach by starting with a commercial diagnostic ultrasound scanner as the foundation.

First, a detailed description of the system will be given, including design considerations and intended applications, followed by a theoretical development for beam simulations and temperature predictions. Parameters relevant to tissue heating such as 3-D intensity distribution are characterized and compared to predictions. Results from both *in vitro* and *in vivo* experiments are presented to highlight the capabilities of the system for tissue heating, and theoretical temperature predictions are also explored. More detail on the design and testing of the therapy arrays can be found in [18].

II. Ultrasound Tissue Heating System

A. Design Considerations and System Overview

Our intended application of the mild-hyperthermia system is to generate mild heating of superficial tumors in small tumors grown in mice, rats and rabbits, with eventual translation to human breast tumors and other superficial cancers. The target tumor size range in our animal models is no larger than 1.5 cm in any dimension, with a typical size on the order of 5 mm in any given dimension for a volume of ~0.1 cm^3. A requirement of the system is to heat a (5 $mm)^3$ region to 42°C in less than 3 minutes (at least 5ºC temperature rise), and maintain the temperature within 0.5 °C for minutes in a controlled manner. Thus, a larger tumor is treated piecewise by directing the beam to individual regions using ultrasound guidance. An important requirement of the tissue heating system is that it is easy to use for high-throughput experiments. A feature that assists high-throughput treatment is integration of imaging and therapy into the same system. The imaging allows co-location of the tumor, the temperature feedback device, and the therapy beam.

In starting with a clinical scanner as the foundation, we are able to take advantage of the following benefits: ease of use, the availability of optimized and cost-effective imaging arrays, optimized imaging for target tissue, real-time imaging, 4-D capability, ergonomics, FDA approval of the core imaging system and an enormous installed user base familiar with the user interface.

There are challenges as well in integrating therapy within a clinical scanner; these include: the development of new software modes for image-controlled therapy, limited transmitter power output, the development of therapeutic arrays, the requirement for co-localization of imaging and therapy beams, integration of temperature feedback and acoustic control, and treatment planning.

NIH-PA Author Manuscript

NIH-PA Author Manuscript

NIH-PA Author Manuscript

An overview schematic of the system is shown in Figure 1. The system consists of a Siemens Antares (Siemens Health Care, Inc., Ultrasound Division, Mountain View, CA), with software modifications, a custom array transducer termed a co-linear array, a temperature measurement system, a control system, and a feedback path into the scanner.

B. Co-linear Array

The co-linear array consists of three parallel transducer arrays. The two outermost arrays operate at a center frequency of 1.5 MHz and the center array operates at a center frequency of 5 MHz. The co-linear geometry was chosen based on several considerations. First, the fixed alignment of the therapy arrays and the imaging array established at manufacturing is advantageous compared to other approaches that utilize separate arrays that require periodic alignment or bulky fixtures. Second, the center imaging array is a standard array optimized for imaging, which greatly simplifies software integration and minimizes cost. Third, two therapy arrays double the effective aperture for tissue heating, yet all three arrays remain within the footprint of a large imaging array making the probe easy to position and not obtrusively large. Lastly, all three arrays must fit within the 192 channel count limitation of the Siemens Antares scanner. Consequently, the choice of a standard 128-element imaging array leaves 64 remaining channels for the therapy arrays.

The two therapy arrays each consist of 64 elements with 0.625-lamba pitch (at 1.54 MHz; c=1500 m/s), which are electrically tied together in parallel, e.g. the nth element on each array shares an electrical connection. The elements are 0.560 mm in azimuth and 6 mm in elevation, with a 40 μm kerf in azimuth and a 0.5 mm kerf in elevation, which results in 4.3 cm^2 of aperture area available for radiation. For these arrays, a single layer of PZT was chosen, which increases the array impedance by a factor of nine as compared with previous designs [18]. A graphite-loaded polymer was used for the front matching layer in order to improve thermal dissipation and thermistors (model 2K7MCD1, BetaTHERM Corporation, Shrewsbury, MA) were included within the matching layers[18] .

The overall fractional bandwidth of the therapy arrays is nominally 53%. The tilt angle of the arrays is nominally 10.2 degrees towards the centerline, which establishes a natural beam crossing at 35 mm in depth and results in an effective f/number of ~1 in azimuth and a depth-of-field of less than 1 cm. Simultaneous transmission from each of the therapy arrays results in −3 dB sidelobes in elevation at the array focus. Whereas such sidelobe levels are unacceptable for imaging, they do not create significant temperature profile distortion for heating times on the order of one minute or longer due to thermal diffusion and the relatively close spacing of the sidelobes, just 2.5 mm from the center of the mainlobe in elevation.

The center imaging array consists of 128 elements with 1.1-lambda pitch (at 5.24 MHz; c=1500 m/s), and is functionally equivalent to a Siemens model VF7-3 probe that is optimized for breast and other superficial imaging exams. This probe has a two-way fractional bandwidth of 73%, and an upper limit imaging resolution of ~300 micronsin azimuth at f/1.

C. Diagnostic Scanner and Spatial Control

A Siemens Antares scanner with software modifications serves as the foundation. The software modifications enable the co-linear array functionality for 1.5-MHz high-duty cycle transmission on the outer rows and 5 MHz (up to 7 MHz) imaging on the center row. Spatial control of the 1.5 MHz heating beam is dictated by track-ball control of the pulsed-Doppler cursor in azimuth and range, keeping in mind of the fixed focus in elevation. Additionally, the Diagnostic User Interface (DUI) feature has been enabled, which allows for back-door control of system variables. The DUI is accessed using LabVIEW to initialize the system and to communicate variables during temperature control.

NIH-PA Author Manuscript

NIH-PA Author Manuscript

NIH-PA Author Manuscript

D. Temperature Control

Temperature within tissue is sensed using a 29-gauge needle thermocouple (MT29/2, Physitemp Instruments, Inc., Clifton, NJ) or a 30-gauge needle thermocouple (HYP-1, Omega Engineering, Inc., Stamford, CT). Both thermocouples are T-type and give approximately the same temperature response in focused ultrasound beams, and the former was used for the work presented here. The thermocouples are interfaced to a data acquisition system consisting of SCXI modules in a SCXI-1000 chassis (National Instruments Corp., Austin, TX). The modules include the SCXI-1600 for analog to digital conversion, the SCXI-1125 for signal conditioning and the SCXI-1328 isothermal terminal block. Digital samples from 8 channels are continuously communicated over USB 2.0 to a PC running LabVIEW (National Instruments Corp., Austin, TX). Each channel is band limited to 4 Hz (−3 dB) with an analog, 3rd order Butterworth low pass filter, prior to being sampled at 100 samples-per-second. In addition to interfacing the needle thermocouple, the system was also interfaced to a rectal thermocouple, 2 thermistors embedded close to the 1.5 MHz arrays, and 3 auxiliary thermocouples. The needle thermocouple readings are further bandlimited to 1 Hz using a digital 3rd order IIR Bessel filter prior to being used in the proportional-differential-integral (PID) control loop.

A list of variables shown in the PID loop is given in Table I, and the PID algorithm is shown in Equations 1, 2 and 3. The temperature error term in Equation 1 is given by the set point temperature (T_{SP}) minus the measured temperature (T). The set point temperature is forced to follow a rising exponential with a time constant of 5 seconds, which prevents step-response-like ringing in the measured temperature. The control variable for the PID algorithm given in Equation 2 is duty factor (DF), where 0 corresponds to 0% duty cycle and 1 corresponds to 100% duty cycle. The calculation of DF consists of a standard implementation of proportional feedback (multiplying K_P), a standard trapezoidal integrator for integral feedback (multiplying K_I), and a reduced-bandwidth differential for differential feedback (multiplying K_D) that reduces sensitivity to noise [19]. The additional term in the algorithm is an anti-windup term (multiplying K_{WU}) that prevents the integrator from growing too large, thus reducing overshoot and increasing stability [20]. The DF is also bound as shown in Equation (3). Based on

$$e(i)=T_{SP}(i)-T(i) \tag{1}$$

$$\begin{aligned} DF(i)=&K_P e(i)+\sum_i \Delta t\, K_I \left(\frac{e(i)+e(i-1)}{2}\right)- \\ &K_{WU}(DF_{TH}(i-1)-DF(i-1))+ \\ &\frac{K_D}{6\Delta t}(e(i)-e(i-3)+3(e(i-1)-e(i-2))) \end{aligned} \tag{2}$$

$$DF_{TH}(i)=\begin{cases} DF(i) & DF_{\min}<DF(i)<DF_{\max} \\ DF_{\min} & DF(i)\le DF_{\min} \\ DF_{\max} & DF(i)\ge DF_{\max} \end{cases} \tag{3}$$

extensive experimentation, typical values for K_P, K_I, K_D and K_{WU} are 0.1–0.2, 0.05–0.1, 0.01–0.05 and 0.01, respectively.

The duty factor is converted to a pulse-repetition frequency, which is communicated to the Antares scanner using the DUI. The duty factor is limited to 0.325, which corresponds to 100 cycles at 1.54 MHz at a PRF of 5 kHz. The minimum duty factor is 0.0065, which corresponds

NIH-PA Author Manuscript

NIH-PA Author Manuscript

NIH-PA Author Manuscript

to a PRF of 100 Hz at the same pulse length. For safety, the duty factor is switched to minimum if the needle temperature exceeds 43°C, or if the therapy arrays exceed 40°C during operation, in order to prevent de-lamination.

The PID loop has fairly low computational requirements and executes in real-time on a 1 GHz Intel Pentium™ III processor as temperature samples are input at a 100 Hz sampling rate.

III. Methods

A. Acoustic Measurements

Acoustic pressure measurements for the 1.5-MHz outer rows were measured using a calibrated 500-μm diameter needle hydrophone (Müller-Platte Needle Probe, ONDA Inc., Sunnyvale, CA) in distilled, deionized and degassed water. For all acoustic measurements, the ultrasound scanner was configured in pulsed-Doppler mode to transmit 100-cycle pulses to a single line-of-sight with a PRF of 100 Hz, focused at a 35 mm depth. Three-dimensional mapping was obtained by scanning the hydrophone in a rectilinear format using an XYZ motion stage. The acoustic waveforms were digitized using a digital storage oscilloscope and transferred to a PC for processing. A custom pulse current monitor for the transmitter power supply was used as a trigger signal to synchronize data acquisition with pulse transmission. The transmitted voltage was manually controlled via the DUI.

The 3-D acoustic field was sampled at 0.2 mm increments in azimuth, 0.4 mm increments in elevation and 1 mm increments in depth for a total of 10,816 field points. For each field point, the waveform was digitally filtered to reduce noise, and the envelope detected using the Hilbert transform. The acoustic intensity was determined by squaring the envelope and calculating the time-averaged intensity. The resulting 3-D intensity distribution was then upsampled to 0.1, 0.2 and 0.5 mm, respectively, in Matlab (v7.6, Mathworks, Natick, MA). To compensate for the spatial averaging caused by the hydrophone, each azimuth-elevation plane was deconvolved with a 0.5-mm diameter smoothing function. The total acoustic power (TAP) output was measured using a radiation force balance (model UPM-DT-1AV, Ohmic Instruments Co., Easton, MD).

B. In vitro Experiments

The ultrasound heating system was tested on chicken breast purchased fresh and unfrozen at a local grocery store and on extra firm, smooth-textured soy tofu (Silken Extra Firm Tofu, Morinaga Nutritional Foods, Inc., Torrance, CA).

In the first test, chicken was placed into a water bath filled with degassed-deionized water at room temperature. The 29-gauge needle-thermocouple was inserted into the chicken tissue, roughly perpendicular to the central axis of the array and aligned with the array in azimuth as determined by the 5 MHz B-mode image. The chicken was allowed to reach the steady-state temperature of the surrounding water bath. Next, the pulsed-Doppler heating cursor was placed at the tip of the needle, and the temperature controller was enabled and set to a value slightly above the baseline temperature. After at least 15 seconds of steady state temperature, the set point was then increased stepwise by 2°C for 50 seconds, followed by a second increase by 2° C for 50 seconds, after which a final step increase of 2°C was maintained for 65 seconds (for a total of 6°C over baseline). The maximum TAP used in this test was 4.1 W. To demonstrate repeatability, 3 heating trials were performed on the same sample. Prior to averaging temperature profiles and calculating the standard deviation, the initial temperatures for all 3 trials were offset to a value of 20°C.

A second test was performed on tofu. A 25 mm cubic sample of tofu was cut and inserted onto the needle thermocouple, which was rigidly clamped to a 3-D micrometer stage. The tip of the

NIH-PA Author Manuscript

NIH-PA Author Manuscript

NIH-PA Author Manuscript

needle was placed at the center of the cube. The needle was located on the 5 MHz B-mode image and the pulsed-Doppler heating cursor was placed on the tip of the needle and the procedure repeated as above. The water path dimension between the center of the array and tip of the needle was ~23 mm. In addition to the measured temperatures, the predicted temperature was also calculated for the cubic tofu sample using thermal, acoustic and other relevant parameters shown in Table II.

C. In vivo Experiments

The experimental protocol for this study was approved by the UC Davis Animal Care and Use Committee. Three female FVB mice were used. Mouse 1 and 2 were 5 months in age and weighed ~25 g each. Mouse 3 was 2 months old and weighed 20 g. Each was implanted with Met-1 tumor fragments in the 4^{th} right and left mammary fat pads, which is the native environment for this aggressive metastastic breast cancer model [21]. The treated tumors were allowed to mature until their volumes were 0.3, 0.4, and 0.1 cm^3, respectively, as measured using a Siemens ACUSON Sequoia C512 using a 15L8 probe. Each mouse was anesthetized using isofluorane-inhaled anesthesia (2%), and each mouse was shaved using clippers from the chest down to below the tumors and a depilatory cream was applied to remove the remaining hair. A custom fixture was machined to direct the co-linear array vertically-upwards into a 37° C temperature-controlled water bath, filled initially with degassed and deionized water that served as an acoustic standoff. The mouse was placed over the water bath and the tumor was submerged. A rectal thermocouple probe was used to monitor the animal's core temperature. A sterilized 29-gauge needle thermocouple was inserted near the center of the tumor and located on the 5 MHz B-mode image. The temperature controller was enabled and set to 37°C. Once a steady state temperature was achieved for at least 60 seconds, the set point temperature was increased to 42°C for 300 seconds, after which it was reduced back to 37°C. The same procedure was repeated 3 times on mouse 2 in order to assess repeatability.

D. Simulation of 3-D Beam Intensity

Reliable methods exist for calculating acoustic beam functions for ultrasound transducer arrays [22–25]. Much of the recent literature on ultrasound field calculations focuses on wideband ultrasound fields and the influence of nonlinear components for both imaging and thermal therapies. For the purposes of mild-hyperthermia, it is assumed that narrowband insonation will be used in order to minimize peak-negative pressure and the corresponding mechanical index (MI). It has been shown in the literature[26] that the contribution of nonlinear components to heating is small for peak-negative pressures in the vicinity of 2 MPa (less than 2% following[27] and our own spectral measurements at 1.54 MHz), which corresponds to a MI of 1.6 at 1.5 MHz, and we intend to keep the MI at or below the FDA limit of 1.9. Here we consider only monochromatic fields that obey linearity.

The geometry of the outer therapy arrays has been defined and organized according to the conventions used in Field II [23], a free linear ultrasound field simulation software package written in compiled C for use with MATLAB (The Math Works, Inc., Natick, MA). Using the `xdc_linear_multirow()` function, physical elements are sub-divided into mathematical elements, and the acoustic field is calculated for each point in space by summing the contributions from each mathematical element. Coordinate transformations to the individual elements are applied in order to tilt each 1.5 MHz outer row inwards by an arbitrary angle. Focusing delays are calculated for each physical element and applied to the corresponding mathematical elements. The focal point is fixed at 35 mm from the center of each tilted row.

Due to the narrowband nature of the transmitted pulses used in this work, the acoustic field is calculated using the first Rayleigh-Sommerfeld solution[22]:

NIH-PA Author Manuscript

NIH-PA Author Manuscript

NIH-PA Author Manuscript

$$P(\vec{r}_0)=\frac{1}{j\lambda}\iint_{S_1} P(\vec{r}_1)\frac{exp(jk(r_{01}-d(\vec{r}_1)c))}{r_{01}}cos\,\theta\,dS, \tag{4}$$

where $P()$denotes the complex pressure of either the field or aperture, $\vec{r}_0$ is a point in the field, λ is the wavelength, $\vec{r}_1$ is a point on the aperture, λ is the wavelength, k is the wavenumber, $\vec{r}_{01} = |\vec{r}_0 - \vec{r}_1|$, $d(\vec{r}_1)$ is the geometric focusing time delay at $\vec{r}_1$ c is the speed of sound, θ is the angle between the surface normal vector $\vec{n}$ at $\vec{r}_1$ and the vector $\vec{r}_{01} = \vec{r}_0 - \vec{r}_1$, and dS is the area of a mathematical element on surface S_1. The complex pressure field is computed for each point in the field, and the pressure magnitude is computed. Attenuation is included by setting $k=\frac{\omega}{c}+j\alpha$ where ω is the angular frequency, and α is the amplitude attenuation coefficient in Nepers/m. A water path is included by applying tissue attenuation for paths beyond the water-tissue interface and neglecting attenuation in the water path due to the small magnitude at 1.5 MHz.

To increase accuracy, the physical elements are divided into 8 equal parts in elevation and 2 equal parts in azimuth, for a total of 1024 mathematical elements. A further increase in sampling does not alter the result significantly. The 3-D field was calculated with a resolution of 0.25 mm in all 3 dimensions. For the thermal calculations, acoustic intensity is calculated according to:

$$I(\vec{r}_0)=\frac{|P(\vec{r}_0)|^2}{2\rho c}. \tag{5}$$

E. Simulation of 3-D Tissue Heating

The temperature rise was calculated using the finite-difference time-domain (FDTD) method to approximate a solution to the Pennes' Bio-heat Transfer Equation (BHTE) [28] given by:

$$\rho C_p\frac{\partial T}{\partial t}=\nabla\cdot(K\nabla T)+q-b(T-T_b), \tag{6}$$

where ρ is density (Kg m^{-3}), C_p is the specific heat for the tissue (J Kg^{-1} °C^{-1}), T is temperature (°C), t is time (s), ∇ is the spatial gradient operator, K is the thermal conductivity (W m^{-1} ° C^{-1}), q is rate of heat production per unit volume given by $2\alpha I$ (W m^{-3}), α is the acoustic absorption (Np m^{-1}), I is acoustic intensity (W m^{-2}), b is a constant related to blood perfusion (W m^{-3} °C^{-1}), and T_b is the blood temperature (°C).

The FDTD implementation is given by the following second-order finite-difference approximation [29]:

$$\begin{aligned} T^{m+1}(i,j,k)&=T^m(i,j,k)\\ &+\frac{\delta_t}{\rho C_p\delta^2}K[T^m(i+1,j,k)+T^m(i,j+1,k)+T^m(i,j,k+1)+T^m(i-1,j,k)\\ &+T^m(i,j-1,k)+T^m(i,j,k-1)-6T^m(i,j,k)]+\frac{\delta_t}{\rho C_p}q(i,j,k)\\ &-\frac{\delta_t}{\rho C_p}b[T^m(i,j,k)-T_b], \end{aligned} \tag{7}$$

where i, j and k are spatial indexes for each coordinate in 3-D, m is the temporal index, δ_t is the temporal resolution, δ is the spatial resolution. For the purposes of the work presented here,

NIH-PA Author Manuscript

NIH-PA Author Manuscript

NIH-PA Author Manuscript

the boundary conditions are defined to be a constant ambient temperature. To ensure a numerically stable solution, the bound on δ_t is given by [29]:

$$\delta_t \leq \frac{2\rho C_p \delta^2}{12K + b\delta^2}. \quad (8)$$

In order to compare to simulated temperatures to measured temperatures as a function of time, the simulated temporal thermal profiles are passed through a 3rdorder Butterworth IIR with a cutoff of 4 Hz followed by a 3rdorder IIR Bessel filter with a cutoff of 1 Hz.

IV. Results

A. Acoustic Characterization

Figure 2 shows normalized −3 dB intensity isosurfaces rendered in 3-dimensions for measured (a) and simulated (b) beams. The corresponding cutaway views of the beams in the elevation-depth plane are shown in (c) and (d) for (a) and (b), respectively. The cut-away views expose the intensity distribution within the beam down to the −3 dB intensity defined by the isosurface. The −3 dB mainlobe beam dimensions for the measured beam are 1.5 mm in elevation, 1.0 mm in azimuth and 9.0 mm in depth. The sidelobes caused by diffraction in elevation are below 60% of the mainlobe peak. Likewise, the mainlobe beam dimensions for the simulated beam are 1.5 mm in elevation, 1.0 mm in azimuth and 7.5 mm in depth, and the sidelobes are below 55% of the mainlobe peak.

The peak-negative pressure as a function of voltage is shown in Figure 3(a). Likewise, the total acoustic power (TAP) output measured using the radiation force balance is shown in Figure 3 (b). The maximum TAP power output for the current system is 4.1 W, with a corresponding peak-negative pressure of 2.2 MPa. It should be noted that an MI of 1.9 corresponds to a peak-negative pressure of 2.3 MPa at 1.54 MHz.

B. In vitro Experiments

Figure 4 summarizes the results from 3 trials in which insonation produced a six degree temperature increase within chicken breast in operator-requested, graduated increments of 2 degrees, demonstrating the tight control achieved by the PID controller. For the three graduated increases in temperature of 2, 4 and 6 degrees, the set point temperature is reached in 16, 18 and 15 seconds for time-average heating rates of 0.33, 0.25 and 0.13°C/s, respectively. Additionally, the temperature crosses the rising trajectory of the set point temperature at 3.5, 3.4 and 3.3 seconds, respectively, which indicates that the heating rate is limited by the first-order, low-pass response of the set point temperature (time constant = 5 s). The inset plot illustrates the small standard deviation in temperature across 3 repeated trials. The periodic noise in the temperature is due to interleaved B-mode updates, and its fundamental component occurs at a frequency of ~2 Hz. The temperature controller achieved the set point with a worst-case overshoot of 0.2°C for all three steps in the set point and no observable ringing thereafter.

During steady-state control, the temperatures were maintained to within 0.1°C of the set point temperature. The maximum deviation of the duty factor across repeated trials was 6.6% of full scale (0.325=100%).

Figure 5 summarizes the results for 3 trials of tofu heating using the same protocol as for the chicken heating. Additionally, the results of the temperature prediction using parameters in Table II are shown (a), and the difference between the measured temperature and the set point and predicted temperatures (b). For the three graduated increases in temperature of 2, 4 and 6 degrees, the set point temperature was reached in 11, 12 and 16 seconds for time-average

NIH-PA Author Manuscript

NIH-PA Author Manuscript

NIH-PA Author Manuscript

heating rates of 0.18, 0.17 and 0.13°C/s, respectively. During each consecutive increase in the set point temperature, the measured temperature crossed the set point trajectory at 5.2, 7.1 and 3 seconds, respectively; thus indicating that the heating rate is limited by the first-order, low-pass response of the set point temperature as with chicken. The temperature controller achieved the set point temperature with a worst-case overshoot of 0.25°C following a step change in the set point and no observable ringing thereafter. During steady-state control, the temperatures were maintained to within 0.1°C. The temperature prediction tracked the measured temperature to within 0.3°C using published and measured parameters for tofu (Table II), including an absorption coefficient of 16 Np/m. The maximum deviation of the duty factor across repeated trials was 8.6% of full scale (0.325=100%).

C. In vivo Experiments

A screen capture from the modified Antares imaging system during the tumor heating experiment is shown in Figure 6. The 5 MHz B-mode image shows the tumor and thermocouple needle inserted from the right to left (see illustration to the right). The pulsed Doppler cursor is placed near the active tip of the thermocouple needle as shown.

The results from heating 3 mouse tumors are summarized in Figure 7. The top, middle and bottom plots in each set correspond to the temperatures, duty factor and CEM43, respectively, with labeling consistent with previous plots. For mouse 1, 2 and 3, the set point temperature of 42°C is reached in 138, 63 and 148 seconds, for a time average heating rate of 2.2, 4.8 and 2°C/min. The CEM43 thermal dose reached 0.9, 1.1, and 0.9 min, respectively. The slope of the thermal dose in the linear portion of the CEM43 curves is 0.25 min/min (standard deviation=0.002) and virtually identical across all three experiments despite much larger differences in the heating rate. The overshoot following a step increase in set point temperature is limited to 0.2°C, and the temperature is maintained to within 0.2°C for at least 3 minutes at 42°Cin each case.

The variability in the heating over three repetitions of the protocol is shown in Figure 8. The maximum standard deviation across the entire heating profile is 0.27°C. Likewise, the maximum deviation in the duty factor is 0.07 or 22% (0.325=100%). The deviation in CEM43 across all three trials is negligible (not shown).

VI. DISCUSSION AND CONCLUSION

A diagnostic ultrasound scanner was modified to enable spatial and temporal control of tissue heating. An array, combining confocal 1.5 MHz therapeutic arrays with a 5.5 MHz imaging array, facilitates well-controlled hyperthermia in small tumors. The system is capable of achieving and maintaining *in vivo* temperatures of at least 42°C for several minutes and thermal doses significantly exceeding 0.5 CEM43. The focal point of the beam is directed with a high degree of control and freedom, equivalent to pulsed-Doppler, which enables high-throughput treatments on small animal disease models.

The sidelobes in the beam are a consequence of diffraction caused by a gap in the elevational aperture of the dual therapeutic arrays. To obtain close agreement between the measured and simulated beams it was necessary to use a tilt angle of 12.2 degrees instead of the nominal tilt angle of 10.2 degrees, which is partially justified by the proprietary slow-speed lens material covering the tilted arrays. Whereas the sidelobes do contribute to heating, the mainlobe contributes significantly more as the peak intensity is twice as great and the area is much larger. Furthermore, thermal diffusion tends to dominate the temperature distribution and smooth out lumps for the heating durations that we consider. It is known that for long duration heating, the average power delivered over an area is predictive of the heating [5,6].

NIH-PA Author Manuscript

NIH-PA Author Manuscript

NIH-PA Author Manuscript

Temporal control of heating is achieved using a modified PID control system. With minor tuning of the gain factors, it was possible to control temperature indefinitely to better than 0.1° C *in vitro* with overshoots staying within 0.5°C. Such tight temperature control is necessary in mild hyperthermia due to the highly nonlinear dependence of cell survival with temperature as is evident in the Arrhenius-based CEM43 thermal dose measure.

We observed limitations in the thermal feedback system. In all of the heating profiles shown here, peak power (or substantially most of the peak power) is required initially during the heating phase and then reduced as the temperature approaches the goal. This situation is not always the case. For example, in some situations, too much power is available for the commanded temperature increase, which can result in oscillation of the measured temperature. Such situations are readily alleviated by reducing the peak-transmitted power or by reducing the PID gains, particularly the integral gain. To accommodate such situations, the stability of the control system would benefit from adaptive selection of PID gains. Such measures of improving stability over a range of conditions are not uncommon in PID control.

An additional limitation in the current system is that the location of the thermocouple needle relative to the elevational focus must be carefully controlled. It is essential that the needle is located on the ultrasound image and aligned properly. With practice, locating and positioning the needle becomes routine; however, alignment errors are always possible, particularly since imaging resolution in elevation is much less than it is in azimuth for 1-D arrays. Magnetic resonance-based thermometry or ultrasound thermometry in 3-D would eliminate this problem.

Based on known parameters for tofu and the parameters employed by the arrays, the temperature profile predicted by the BHTE closely matches that measured during heating, to within 0.5°C (Fig. 5). Our experience is that longer duration predictions become more difficult as the boundary conditions begin to play a more significant role in the thermal pathway. Additionally, *in vivo* studies involve a mixture of boundary conditions and spatially and/or temporally variable thermal and acoustic parameters, so it is expected that predictions based on a simplified model such as that used for the tofu will deviate from measured values. Consequently, a robust application of a predictive component to the control system requires feedback from one or more sensors and a time-dependent weighting in order to deemphasize old predictions. Our future efforts will focus on incorporating the CEM43 thermal dose metric and a predictive component into the PID algorithm and extending PID from single line-of-sight to scanned beam control in both azimuth and elevation.

The variability observed in the heating profiles was small across repeated phantom and *in vivo* trials, generally within 0.3°C. Greater variability was observed between multiple mouse tumors (Fig. 7). In the former, the small variability is mostly attributable to periodic interleaving of B-mode images during which time the therapy arrays are not transmitting. Our system does not currently allow for simultaneous transmission of therapy and imaging beams, and thus, requires periodic B-mode acquisition. Although the system doesn't allow simultaneous heating and imaging, the effect of the imaging could be mitigated by reducing the frequency of the image collection.

The variability seen between mice in Fig. 7 is potentially explained by small misalignments with the thermocouple relative to the beam and inhomogeneities in acoustic absorption. Hyperemia caused by the tissue heating adds additional, temperature-dependent thermal loss which may partially account for the higher power levels and durations required to heat the tumors compared to the in vitro models. Based on simulations, the volume of tissue that is elevated to within 1 degree of the set point temperature is estimated to be ~0.1 cm^3. In the future, we will report on broad beam insonation for heating larger tissue volumes. Variability

NIH-PA Author Manuscript

NIH-PA Author Manuscript

NIH-PA Author Manuscript

between subjects and the circumstances of each treatment make it all the more important to have a robust, stable, safe and repeatable system for generating mild-hyperthermia.

Acknowledgments

We wish to thank the NIH for their generous support for this project under grant number R01 CA103828. Ed Gardner, Lisa Fearn, and Bill Beck of Siemens Health Care, Inc., Ultrasound Division, and Sanli Ergun and Tom Clary of Siemens Corporate Research, are gratefully acknowledged for their valuable support in the development of the co-linear probes. We also thank Robert Cardiff and Larry Young for providing us with the Met-1 tumors.

References

1. Kim YT, Kim HC, Inada-Kim M, et al. Evaluation of Tissue Mimicking Quality of Tofu for Biomedical Ultrasound. Ultrasound Med Biol. Dec 18;2008
2. Wu JR. Tofu as a tissue-mimicking material. Ultrasound in Medicine and Biology Sep;2001 27(9): 1297–1300. [PubMed: 11597372]
3. O'Brien WD Jr. Ultrasound-biophysics mechanisms. Prog Biophys Mol Biol Jan–Apr;2007 93(1–3): 212–55. [PubMed: 16934858]
4. Wells PN. Review: absorption and dispersion of ultrasound in biological tissue. Ultrasound Med Biol Mar;1975 1(4):369–76. [PubMed: 1098249]
5. O'Brien WD, Ellis DS. Evaluation of the unscanned soft-tissue thermal index. Ieee Transactions on Ultrasonics Ferroelectrics and Frequency Control Nov;1999 46(6):1459–1476.
6. O'Brien WD, Yang Y, Simpson DG. Evaluation of unscanned-mode soft-tissue thermal index for rectangular sources and proposed new indices. Ultrasound in Medicine and Biology Jul;2004 30(7): 965–972. [PubMed: 15313328]
7. Hindley J, Gedroyc WM, Regan L, et al. MRI guidance of focused ultrasound therapy of uterine fibroids: Early results. Am J Roentgenol Dec;2004 183(6):1713–1719. [PubMed: 15547216]
8. Cheng HL, Plewes DB. Tissue thermal conductivity by magnetic resonance thermometry and focused ultrasound heating. J Magn Reson Imaging Nov;2002 16(5):598–609. [PubMed: 12412038]
9. Moonen CTW. Spatio-temporal control of gene expression and cancer treatment using magnetic resonance imaging-guided focused ultrasound. Clin Cancer Res Jun 15;2007 13(12):3482–3489. [PubMed: 17575210]
10. Kong G, Braun RD, Dewhirst MW. Characterization of the effect of hyperthermia on nanoparticle extravasation from tumor vasculature. Cancer Res Apr 1;2001 61(7):3027–3032. [PubMed: 11306483]
11. Song CW, Park HJ, Lee CK, et al. Implications of increased tumor blood flow and oxygenation caused by mild temperature hyperthermia in tumor treatment. Int J Hyperther Dec;2005 21(8):761–767.
12. Jones EL, Prosnitz LR, Dewhirst MW, et al. Thermochemoradiotherapy improves oxygenation in locally advanced breast cancer. Clin Cancer Res Jul 1;2004 10(13):4287–4293. [PubMed: 15240513]
13. Sun Y, Sugawara M, Mulkern RV, et al. Simultaneous measurements of temperature and pH in vivo using NMR in conjunction with TmDOTP5- NMR Biomed Dec;2000 13(8):460–466. [PubMed: 11252031]
14. Westermann AM, Jones EL, Schem BC, et al. First results of triple-modality treatment combining radiotherapy, chemotherapy, and hyperthermia for the treatment of patients with stage IIB, III, and IVA cervical carcinoma. Cancer Aug 15;2005 104(4):763–770. [PubMed: 15968685]
15. Needham D, Anyarambhatla G, Kong G, et al. A new temperature-sensitive liposome for use with mild hyperthermia: Characterization and testing in a human tumor xenograft model. Cancer Res Mar 1;2000 60(5):1197–1201. [PubMed: 10728674]
16. Dewhirst MW, Viglianti BL, Lora-Michiels M, et al. Basic principles of thermal dosimetry and thermal thresholds for tissue damage from hyperthermia. Int J Hyperthermia May-Jun;2003 19(3): 267–94. [PubMed: 12745972]
17. Dewhirst MW, Vujaskovic Z, Jones E, et al. Re-setting the biologic rationale for thermal therapy. International Journal of Hyperthermia 2005;21(8):779–790. [PubMed: 16338861]

NIH-PA Author Manuscript

NIH-PA Author Manuscript

NIH-PA Author Manuscript

18. Stephens DN, Kruse DE, Ergun AS, et al. Efficient array design for sonotherapy. Phys Med Biol Jul 21;2008 53(14):3943–69. [PubMed: 18591737]

19. Galan P. Enhanced temperature controller is both fast and precise. Edn Mar 1;2001 46(5):111–120.

20. Bohn C, Atherton DP. An Analysis Package Comparing Pid Antiwindup Strategies. IEEE Contr Syst Mag Apr;1995 15(2):34–40.

21. Lin EY, Jones JG, Li P, et al. Progression to malignancy in the polyoma middle T oncoprotein mouse breast cancer model provides a reliable model for human diseases. Am J Pathol Nov;2003 163(5): 2113–2126. [PubMed: 14578209]

22. Goodman, JW. Introduction to Fourier optics. 3. Englewood, Colo: Roberts & Co; 2005.

23. Jensen JA. Simulation of advanced ultrasound systems using Field II 1:636–639.

24. Jensen JA, Svendsen NB. Calculation of pressure fields from arbitrarily shaped, apodized, and excited ultrasound transducers. IEEE T Ultrason Ferr 1992;39(2):262–267.

25. McGough RJ. Rapid calculations of time-harmonic nearfield pressures produced by rectangular pistons. Journal of the Acoustical Society of America May;2004 115(5):1934–1941. [PubMed: 15139602]

26. Hallaj IM, Cleveland RO. FDTD simulation of finite-amplitude pressure and temperature fields for biomedical ultrasound. Journal of the Acoustical Society of America May;1999 105(5):L7–L12. [PubMed: 10335650]

27. Goss SA, Fry FJ. Non-Linear Acoustic Behavior in Focused Ultrasonic Fields - Observations of Intensity Dependent Absorption in Biological Tissue. Ieee Transactions on Sonics and Ultrasonics 1981;28(1):21–26.

28. Pennes HH. Analysis of Tissue and Arterial Blood Temperatures in the Resting Human Forearm. Journal of Applied Physiology 1948;1(2):93–122. [PubMed: 18887578]

29. Wang JQ, Fujiwara O. FDTD computation of temperature rise in the human head for portable telephones. Ieee Transactions on Microwave Theory and Techniques Aug;1999 47(8):1528–1534.

NIH-PA Author Manuscript

NIH-PA Author Manuscript

NIH-PA Author Manuscript

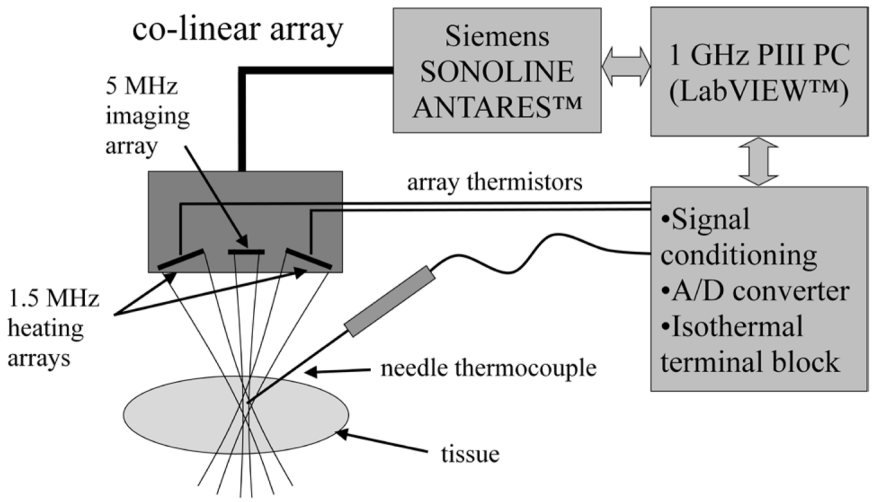

Figure 1.
Schematic representation of controlled tissue heating system.

NIH-PA Author Manuscript

NIH-PA Author Manuscript

NIH-PA Author Manuscript

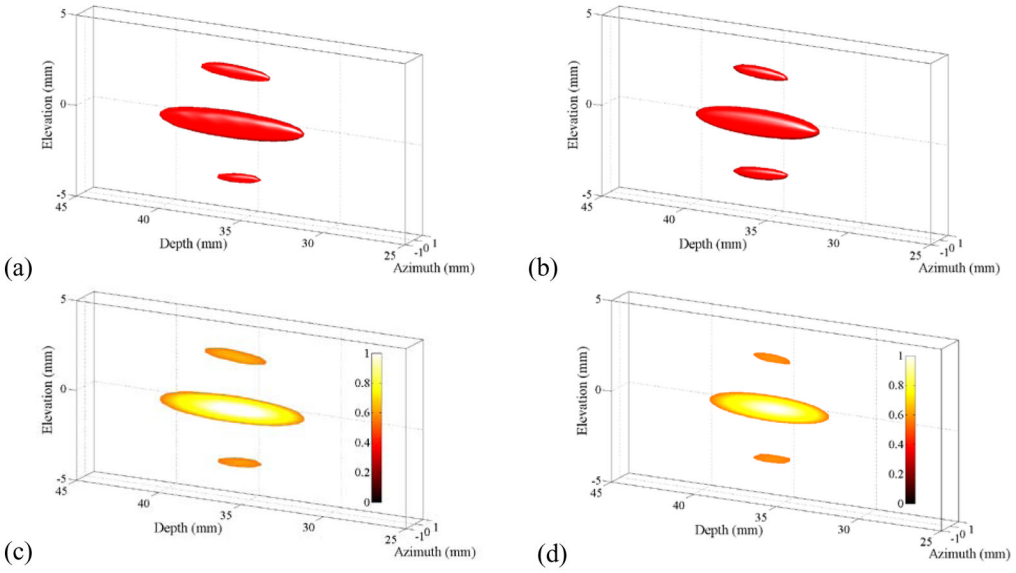

Figure 2.

Half-intensity beam isosurfaces for measured (a) and simulated (b) beams in water with corresponding cutaway views in (c) and (d). In each plot, the transducer array points from left to right. In (c) and (d), the linear color scale denotes normalized power. The prominent elevation side lobes are a natural consequence of interference caused by the split aperture.

NIH-PA Author Manuscript

NIH-PA Author Manuscript

NIH-PA Author Manuscript

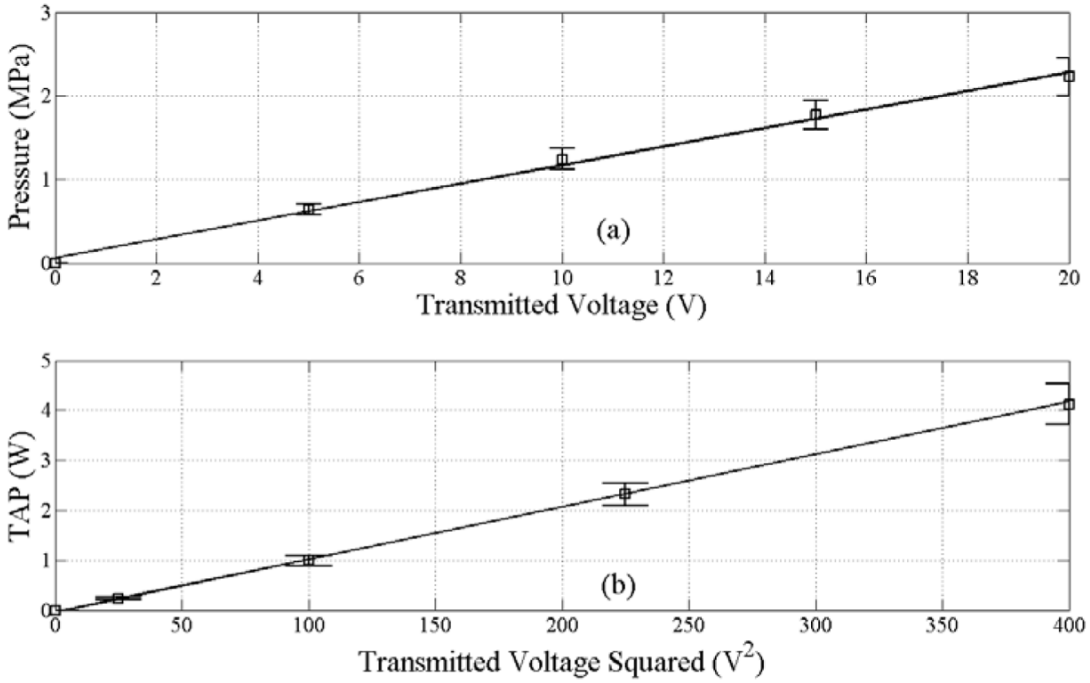

Figure 3.

Acoustic measurements for the co-linear array of peak-negative pressure (PNP, a) obtained using a 0.5 mm hydrophone at a focal depth of 35 mm and TAP (b) obtained using a radiation force balance at 32.5% duty cycle. An MI of 1.9 corresponds to a PNP of 2.3 MPa at 1.5 MHz. The error bars indicate a 10% uncertainty in the measurements.

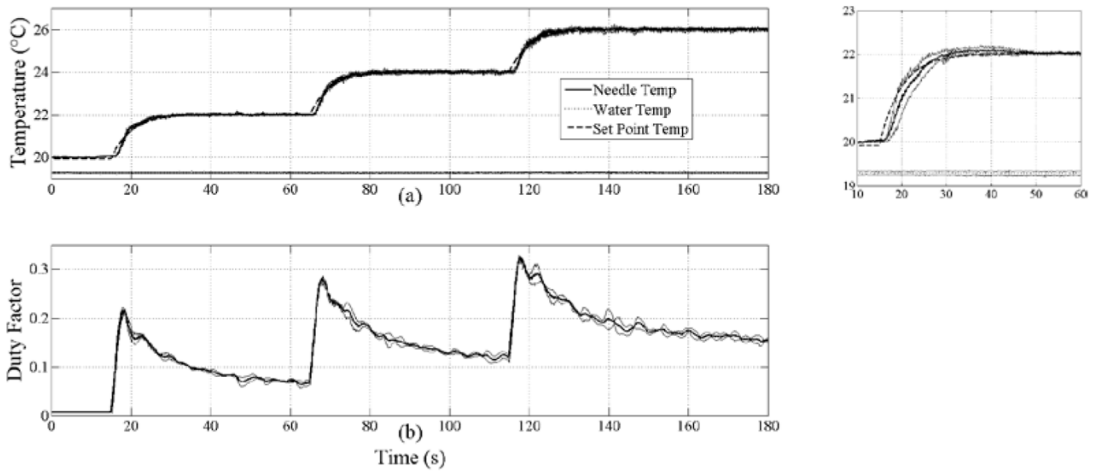

Figure 4.

Average temperature profiles from 3 trials versus time for chicken heating (a) and commanded duty factor (b). In (a), the thermocouple needle (solid), water (dotted) and set point (dashed) temperatures are plotted. Thin solid lines plotted around the needle temperature, water temperature and duty factor curves denote ±1 standard deviation. Inset plot to the right of (a) shows a magnified view of the first heating step from 10 to 60 s. Note that the standard deviation around the needle temperature is small, within 0.25°C over the entire duration. The maximum duty factor of 0.325 corresponds to 4.1 W TAP.

NIH-PA Author Manuscript NIH-PA Author Manuscript NIH-PA Author Manuscript

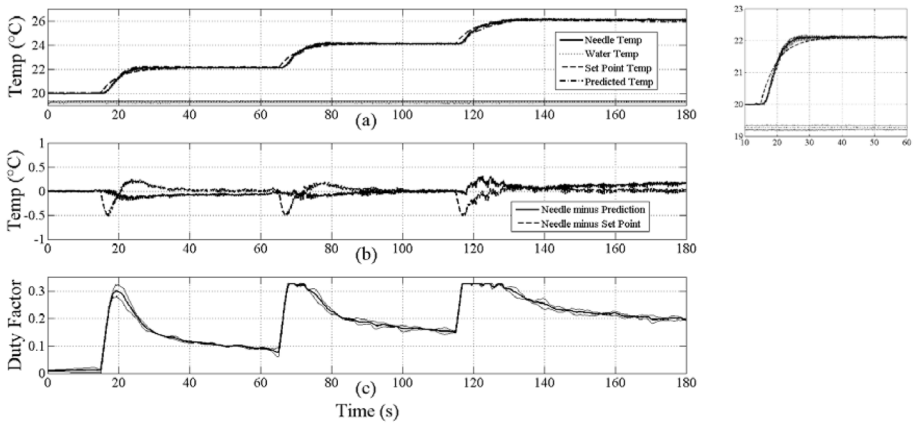

Figure 5.

Average temperature profiles from 3 trials versus time for tofu heating (a), difference profiles between average needle, set point and prediction (b), and commanded duty factor (c). In (a), the thermocouple needle (solid), water (dotted), set point (dashed) and predicted temperatures (dash-dot) are plotted. Thin solid lines plotted around the needle temperature, water temperature and duty factor denote ±1 standard deviation. Inset plot to the right of (a) shows a magnified view of the first heating step from 10 to 60 s. Note that the deviation around the needle temperature is small, within 0.17°C. The maximum duty factor of 0.325 corresponds to 4.1 W TAP.

NIH-PA Author Manuscript NIH-PA Author Manuscript NIH-PA Author Manuscript

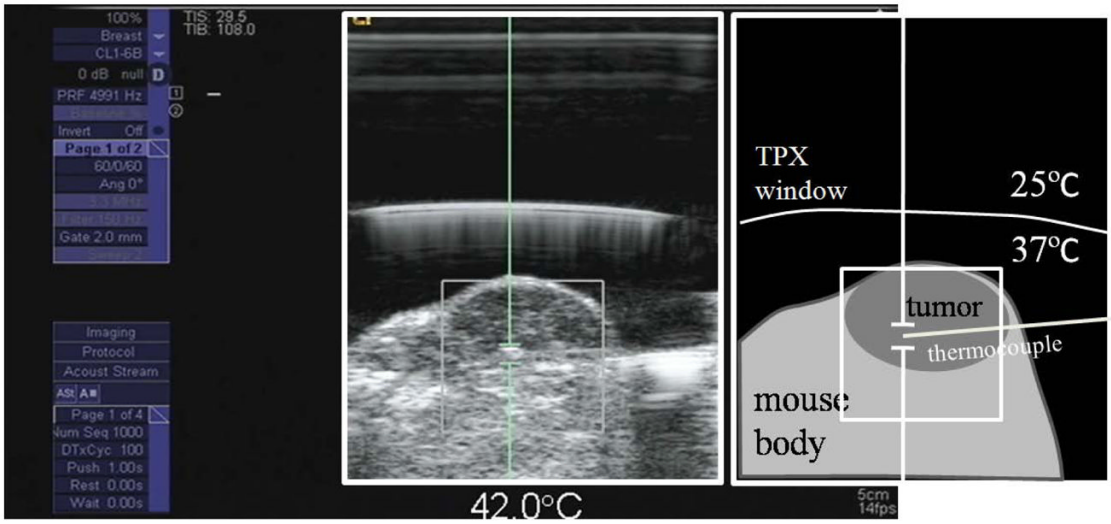

Figure 6.

A screen capture showing a B-mode image of a 4 cm^3 mouse tumor and directed heating using the pulsed Doppler cursor. The cartoon on the right identifies important features, including the TPX (Westlake Plastics Company, Lenni, PA) acoustic window, which separates the cooling water in physical contact with the array face from the heated water in physical contact with the mouse.

NIH-PA Author Manuscript NIH-PA Author Manuscript NIH-PA Author Manuscript

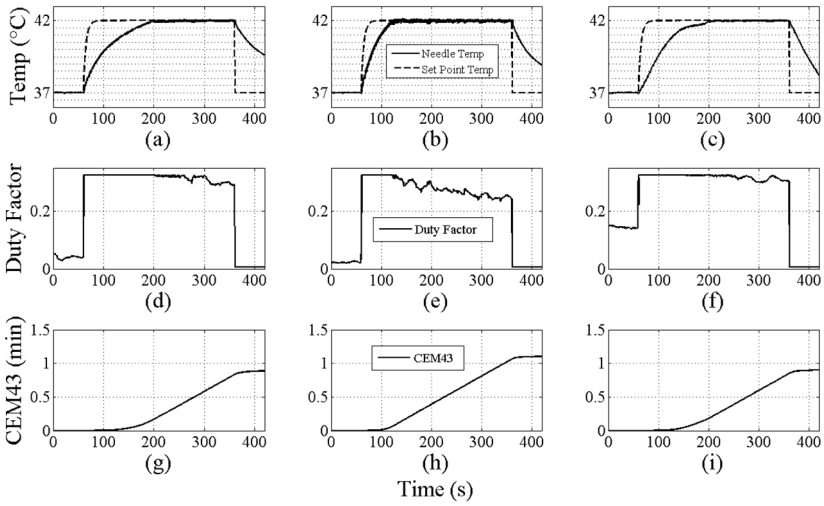

Figure 7.

Temperature profiles, duty factor and CEM43 for mouse 1 (a), (d) and (g); mouse 2 (b), (e) and (h); and mouse 3 (c), (f) and (i), respectively. In (a), (b) and (c), the thermocouple needle (solid) and set point temperatures (dashed) are plotted. In each case, a CEM43 dose of 0.5 minutes is obtained after maintaining 42°C for 60 seconds. The maximum duty factor of 0.325 corresponds to 4.1 W TAP.

NIH-PA Author Manuscript NIH-PA Author Manuscript NIH-PA Author Manuscript

NIH-PA Author Manuscript

NIH-PA Author Manuscript

NIH-PA Author Manuscript

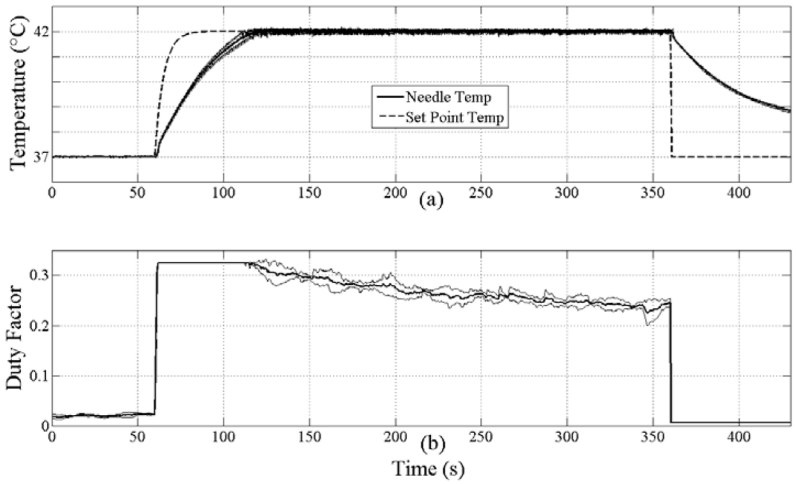

Figure 8.

Average temperature profiles from 3 heating trials on mouse 2 versus time for tumor heating (a) and commanded duty factor (b). In (a), the thermocouple needle (solid) and set point temperatures (dashed) are plotted. Thin solid lines plotted around the needle temperature and duty factor denote ±1 standard deviation. Note that the deviation around the needle temperature is small, within 0.27°C. The maximum duty factor of 0.325 corresponds to 4.1 W TAP.

NIH-PA Author Manuscript

NIH-PA Author Manuscript

NIH-PA Author Manuscript

TABLE I

PID Variables

Variable	Definition
i	Time index
Δt	Sampling interval
$T(i)$	Measured temperature
$T_{SP}(i)$	Set point temperature
$e(i)$	Temperature error
K_P	Proportional gain
K_I	Integral gain
K_D	Differential gain
K_{WU}	Windup gain
$DF(i)$	Duty factor (control variable)
DF_{MIN}	Minimum duty factor
DF_{MAX}	Maximum duty factor
DF_{TH}	Thresholded duty factor

NIH-PA Author Manuscript

NIH-PA Author Manuscript

NIH-PA Author Manuscript

TABLE II

Simulation Variables for Tofu

Variable	Definition	Value	Reference
ρ	Density	1050 kg m^{-3}	measured;[1,2]
C_p	Specific heat capacity	3180 J kg^{-1} °C^{-1}	[1]
K	Thermal conductivity	0.6 W m^{-1} °C^{-1}	[8]
b	Perfusion constant	0 W m^{-3} °C^{-1}	known
α	Acoustic absorption	16 Np m^{-1} (1.54 MHz)	[1,2]
c	Speed of sound	1507 m s^{-1}	measured; [1,2]
δ	Spatial resolution	0.25 mm	known
δ_t	Temporal resolution	0.0574 s	calculated from (4)
I_{SPTA}	Spatial-peak temporal- average intensity	46.5 W cm^{-2}	measured in water